Realizing *zT* > 2.3 in Ge$_{1-x-y}$Sb$_x$In$_y$Te *via* Reducing the Phase-Transition Temperature and Introducing Resonant Energy Doping

Min Hong, Zhi-Gang Chen,* Lei Yang, Yi-Chao Zou, Matthew S. Dargusch, Hao Wang, and Jin Zou*

Dr. M. Hong, Prof. Z.-G. Chen, Dr. L. Yang, Dr. Y.-C. Zou, Prof M.S. Dargusch, Prof. J. Zou

Materials Engineering, The University of Queensland, Brisbane, Queensland 4072, Australia

Email: zhigang.chen@uq.edu.au, j.zou@uq.edu.au

Dr. M. Hong, Prof. Z.-G. Chen, Prof H. Wang

Centre of Future Materials, The University of Southern Queensland, Springfield, Queensland 4300,

Australia

WILEY-VCH

Abstract

GeTe with rhombohedral-to-cubic phase transition is a promising lead-free thermoelectric candidate. Herein, theoretical studies reveal that cubic GeTe has superior thermoelectric behavior which is linked to (1) the two valence bands to enhance the electronic transport coefficients and (2) stronger enharmonic phonon-phonon interactions to ensure a lower intrinsic thermal conductivity. Experimentally, based on $Ge_{1-x}Sb_xTe$ with optimized carrier concentration, a record-high figure-of-merit of 2.3 is achieved *via* further doping with In, which induces the distortion of the density of states near the Fermi level. Moreover, Sb and In co-doping reduces the phase-transition temperature to extend the better thermoelectric behavior of cubic GeTe to low temperature. Additionally, electronic microscopy characterization demonstrates grain boundaries, a high-density of stacking faults, and nanoscale precipitates, which together with the inevitable point defects result in a dramatically decreased thermal conductivity. The fundamental investigation and experimental demonstration provide important direction for the development of high-performance Pb-free thermoelectric materials.

Thermoelectric materials enable the direct heat-to-electricity conversion. Research into these materials has attracted worldwide attention for applications in power generation, waste heat recovery, and refrigeration.[1] Enhancement of the thermoelectric conversion efficiency at a given temperature (T) involves the synergetic management of Seebeck coefficient (S), electrical conductivity (σ), and thermal conductivity (κ, comprising electron (κ_e) and lattice (κ_l) components).[2,3] Accordingly, the dimensionless figure-of-merit ($zT = S^2\sigma T/\kappa$) has been defined to evaluate thermoelectric performance.[4] An eligible thermoelectric material requires a high power-factor ($S^2\sigma$) and a low κ_l, which are related to the transport of charge carriers and phonons, respectively.[5] To ensure a high $S^2\sigma$, strategies including resonant state doping,[6] minority carrier blocking,[7,8] band engineering,[9-11] reversible phase transition,[10,12] and charger carrier scattering modification[13-15] have been widely deployed. On the other hand, to obtain a low κ_l, intrinsic anharmonicity,[16,17] nanostructuring,[18,19] hierarchical architecturing,[20,21] and the development of a matrix with nanoprecipitates[22-25] are generally applied.

Classified as a Pb-free chalcogenide, GeTe has been widely studied as a promising mid-temperature thermoelectric candidate.[26] GeTe undergoes a ferroelectric phase transition, in which the low-temperature rhombohedral (with a space group of R3m) structure (R-GeTe) transforms to the cubic (with a space group of Fm$\overline{3}$m) structure (C-GeTe) at the critical temperature (T_c) of 600 - 700 K.[27] Pristine GeTe is a highly degenerated p-type semiconductor with room-temperature carrier concentration (n) as high as ~10^{21} cm^{-3} due to the considerable Ge deficiency,[16] resulting in a large κ_e but a small $S^2\sigma$. Consequently, the primary requirement of pursuing high thermoelectric performance in GeTe is to reduce n. Similar to other rock-salt group IV chalcogenides, C-GeTe has two valence bands (VBs) with a small energy offset (ΔE), which however transfer into multi sub-valence bands separated by a large ΔE in the R-GeTe material.[28] Therefore, the total band degeneracy of C-GeTe is larger than that of R-GeTe, leading to a higher quality factor in C-GeTe, which is beneficial to secure high thermoelectric performance.[29,30] Accordingly, reducing T_c is a key approach to enhance thermoelectric performance of GeTe by extending the transport behavior of C-GeTe into the low-temperature regime.

Although two VBs in the rock-salt group IV chalcogenides are responsible for the achieved extraordinary thermoelectric performance,[1,31] the formation of secondary VB has been rarely studied, which is due to the fact that most rock-salt group IV chalcogenides are stable over the working temperature range. Favorably, the rhombohedral-to-cubic phase transition of GeTe provides scientific insights into the role of secondary VB in increasing thermoelectric performance, which enlightens the enhancement in thermoelectric properties among a broad range of material systems.

In this study, we achieve a peak $zT \approx 2.3$ stabilizing from 650 to 780 K and an average zT (zT_{avg}) of 1.6 over a working temperature range from 300 to 780 K in GeTe-based alloys via co-doping of Sb and In. Our detailed density functional theory (DFT) calculations, electron and phonon transport modeling studies, and transmission electron microscopy (TEM) investigations disclose that the obtained record-high zT is synergistically due to (1) the optimized n resulted from Sb doping, (2) reduced T_c caused by the co-doping of Sb and In, (3) distorted density of states (DOS) near the Fermi level (E_f) due to the In doping, and (4) a high density of stacking faults and nanoscale precipitates

3

achieved by structural engineering. Although the individual doping of Sb and In in GeTe was studied,[16,32,33] co-doping of Sb and In to yield such a record-high zT in GeTe-based alloys has never been reported. The progress towards enhancing thermoelectric performance in this study encourages the development of super-high thermoelectric performance in wider material systems by co-doping with different elements to modify material properties.

On the basis of lattice parameters of GeTe determined from *in-situ* temperature-dependent X-ray different (XRD) patterns (**Figure S1**b, Supporting Information), we calculate band structures with spin-orbital coupling (SOC) throughout the temperature range of 300 and 780 K, and the results are enclosed in the Video within Supporting Information. As can be seen, the VB maximum switches from the Σ point to the L point during the rhombohedral-to-cubic phase transition, leaving behind a secondary VB_Σ in the C-GeTe. To examine the band degeneracy, we further calculated the Fermi surface. Figure 1a shows the calculated results, in which R-GeTe has 6 full valleys of VB_Σ while C-GeTe has 12 full valleys of VB_Σ plus 8 half valleys of VB_L, suggesting that C-GeTe has a larger band degeneracy. Note that the calculated band structure and Fermi surface are based on the primitive cells of R-GeTe and C-GeTe (refer to Figure S2, Supporting Information), which are similar in the lattice configuration so that the first Brillouin zone is nearly identical for both R-GeTe and C-GeTe. To study the evolution of E_g and ΔE with T, we derive their values, and Figure 1b shows these plots. At 300 K, the direct E_g of R-GeTe is 0.47 eV, which agrees with reference calculated E_g values for GeTe by considering SOC.[34,35] The observed uptrend of E_g with increasing the temperature for each phase is beneficial to suppress bipolar conduction.[36] ΔE of R-GeTe fluctuates around 0.15 eV, which is too large to adopt the electronic contribution from the secondary VB_L. Advantageously, ΔE of C-GeTe is only 0.068 eV near T_c and demonstrates a declining trend with elevating T. Therefore, the presence of VB_L and VB_Σ with smaller ΔE in C-GeTe can lead to higher thermoelectric performance. Detailed discussion on band structure (refer to Section 4, Supporting Information) suggests that VB_L is governed by Ge_$4s^2$ lone pair electrons and that the variation of the VB_L in energy originates from the evolution of such cation s^2 lone pair electrons in trigonal and octahedral coordination during the rhombohedra-to-cubic phase transition.[37]

To qualitatively study the effect of observed two VBs on thermoelectric behavior, we calculate thermoelectric properties as a function of reduced E_f (η) for *p*-type GeTe. $S^2\sigma$ and zT are plotted in Figure 1c and d, respectively. A two-band model considering contributions from the conduction band (CB) and VB_Σ, and a three-band model including tensors of CB, VB_Σ, and VB_L are employed for R-GeTe (blue solid curves) and C-GeTe (red solid curves), respectively. $S^2\sigma$ and zT of C-GeTe are much higher than those of R-GeTe, indicating that C-GeTe is the preferred GeTe phase with higher thermoelectric performance. As a comparison, we also calculate the total contribution from CB and VB_Σ within C-GeTe (pink dash curve). The significant differences of $S^2\sigma$ and zT for this phase determined from the CB+VB_Σ and CB+VB_Σ+VB_L models are caused by contributions from the VB_L, revealing the paramount role of the VB_L in enhancing thermoelectric performance of GeTe. Therefore, C-GeTe has better electronic transport, suggesting that reducing T_c can indeed enhance the overall thermoelectric performance by extending the thermoelectric behavior of C-GeTe to the low-temperature range. Experimentally, T_c of $Ge_{1-x-y}Sb_xIn_yTe$ decreases with increasing doping contents, confirmed by differential scanning calorimetry (DSC) curves for GeTe, $Ge_{0.9}Sb_{0.1}Te$, and $Ge_{0.89}Sb_{0.1}In_{0.01}Te$ and *in-situ* temperature-dependent XRD patterns for GeTe and $Ge_{0.89}Sb_{0.1}In_{0.01}Te$

(Figure S1, Supporting Information). The observed T_c reduction in doped-GeTe is consistent with previously reported results.[16,38]
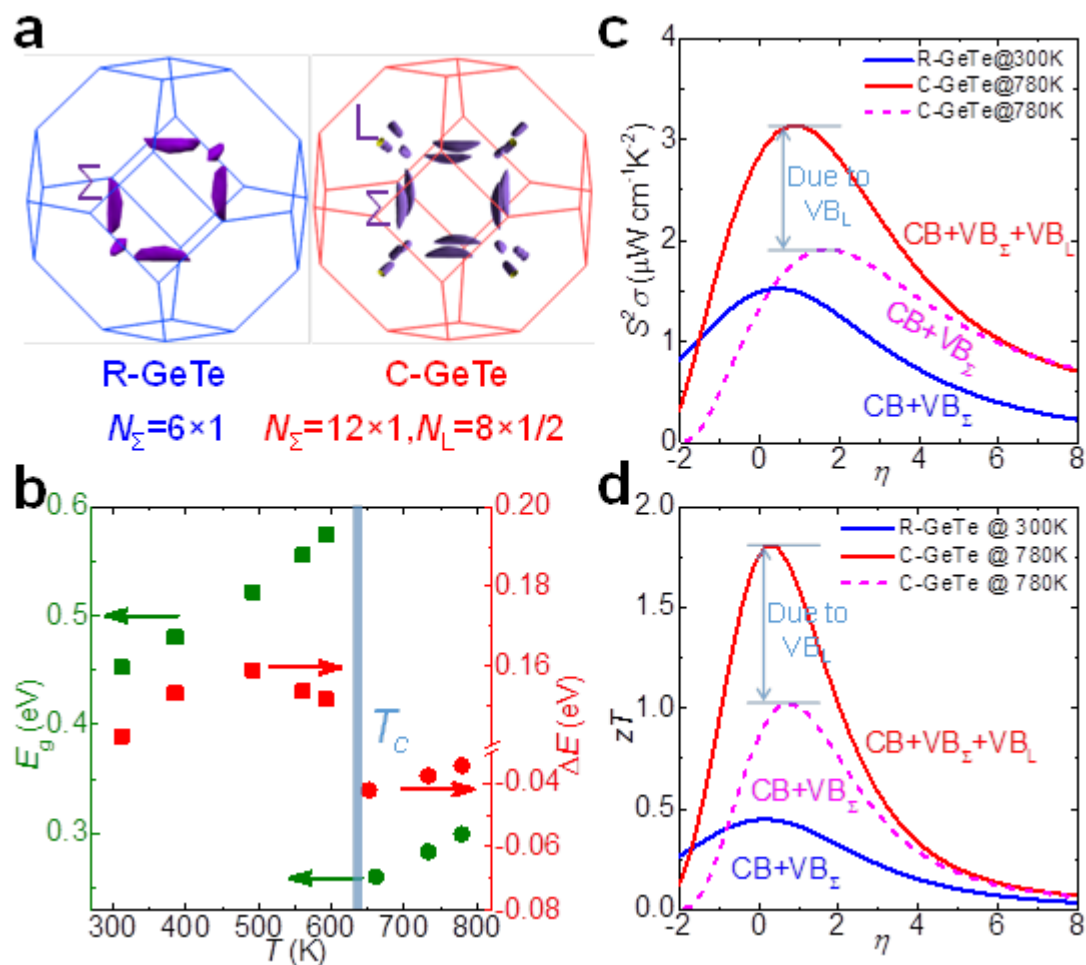

Figure 1 Band structure features of rhombohedral (R-) and cubic (C-) GeTe and the accordingly predicted thermoelectric performance. (a) Calculated Fermi surface of R- and C-GeTe with spin-orbital coupling (SOC). (b) Determined temperature-dependent band gap (E_g) and energy offset (ΔE) between valence band valleys at Σ (VB$_\Sigma$) and at L (VB$_L$) based on the calculated band structures with SOC of GeTe over temperature range of 300 to 800 K with the blue vertical line indicating critical temperature (T_c) of phase transition. Calculated power-factor ($S^2\sigma$) (c) and figure-of-merit (zT) (d) for R- and C-GeTe at 300 K and 780 K, respectively. A two-band model (conduction band (CB) +VB$_\Sigma$) and a three-band model (CB+VB$_\Sigma$+VB$_L$) are used for R- (blue solid curves) and C-GeTe (red solid curves), respectively. As a comparison, contribution excluding VB$_L$ for C-GeTe is also calculated (pink dash curves). To calculate zT, lattice thermal conductivity (κ_l) is obtained from the experimental value for GeTe at 300 K and 780 K in the following discussion.

Figure 2a shows the composition-dependent σ as a function of temperature, which generally decreases with elevating T. Moreover, σ decreases substantially with increasing the Sb content, which is mainly caused by the effectively decreased Hall carrier concentration (n_H) (refer to Figure S6, Supporting Information) due to Sb doping. As can be seen from Figure 2a, further doping with In does not notably modify σ. Figure 2b plots composition-dependent S against T. The positive sign of S

for all $Ge_{1-x-y}Sb_xIn_yTe$ discloses their *p*-type nature and *S* increases with increasing the Sb and In contents. Specifically, at 300 K, *S* of 31 µV K^{-1} in the pristine GeTe increases to 155 µV K^{-1} in $Ge_{0.88}Sb_{0.12}Te$, and further increases to 190 µV K^{-1} in $Ge_{0.888}Sb_{0.1}In_{0.012}Te$. The increase in *S* caused by the Sb doping is due to the decreased n_H to lower E_f.[29] The further increase in *S* due to the In doping can be attributed to resonant energy level doping (discussed later). Furthermore, there are two peaks in the temperature-dependent *S* among $Ge_{1-x-y}Sb_xIn_yTe$ with x > 0.1. While the second peak is caused by the bipolar conduction, the first peak is due to the valence band switch in energy at Σ and L points, associated with the phase transition.[28] The first peak of *T*-dependent *S* generally shifts to lower temperature with increasing the Sb and In contents, indicative of the decrease in T_c Figure 2c plots the variation of $S^2\sigma$. With increasing the Sb content up to 0.1 in $Ge_{1-x}Sb_xTe$, $S^2\sigma$ is enhanced. Upon such an optimal composition, doping In further enhances $S^2\sigma$. Specifically, the maximum $S^2\sigma \approx$ 38 µW cm^{-1}K^{-2} is obtained in $Ge_{0.89}Sb_{0.1}In_{0.01}Te$ at 650 K.

Figure 2d shows *κ versus* the temperate, in which *κ* initially decreases and then slightly increases with increasing the temperature and *κ* declines remarkably with increasing doping contents. The lowest $\kappa \approx 0.92$ W m^{-1}K^{-1} is realized in $Ge_{0.888}Sb_{0.1}In_{0.012}Te$ at 475 K, in contrast with that of 4.2 W m^{-1}K^{-1} for the pristine GeTe at the same temperature. The component breakdown of *κ* using the Wiedemann–Franz law[39] reveals a prominent decline in κ_e, which partially accounts for the decreased *κ* (refer to Section 7 of Supporting Information for the determination of κ_e and κ_l). Plus, the considerably reduced κ_l allows for a further decrease in *κ* (Figure 2e). The decline in κ_e originates from the decreased *σ* (refer to Figure 2a), whereas the reduced κ_l is caused by strengthened phonon scattering (discussed later).

Figure 2f shows *zT* as a function of temperature, in which a maximum $zT \approx 2.3$ is implemented in $Ge_{0.89}Sb_{0.1}In_{0.01}Te$ throughout 650 to 780 K, which is much higher than the peak *zT* of 0.9 at 700 K for the pristine GeTe. The reproducibility of the obtained maximum *zT* has been confirmed by measurements of thermoelectric properties from five independently sintered pellets with the identical nominal composition of $Ge_{0.89}Sb_{0.1}In_{0.01}Te$ (details shown in Figure S8, Supporting Information).

Comparison between our peak *zT* with previously reported values for the state-of-the-art thermoelectric materials illustrates that our $Ge_{0.89}Sb_{0.1}In_{0.01}Te$ material is positioned as one of the top materials from the perspective of thermoelectric performance. In particular, our maximum $zT \approx$ 2.3 stabilizes at the temperature beyond 650 K, yielding a $zT_{avg} \approx 1.6$ over the working temperature range of 300 to 780 K, higher than most reported thermoelectric candidates (refer to Figure S10, Supporting Information).
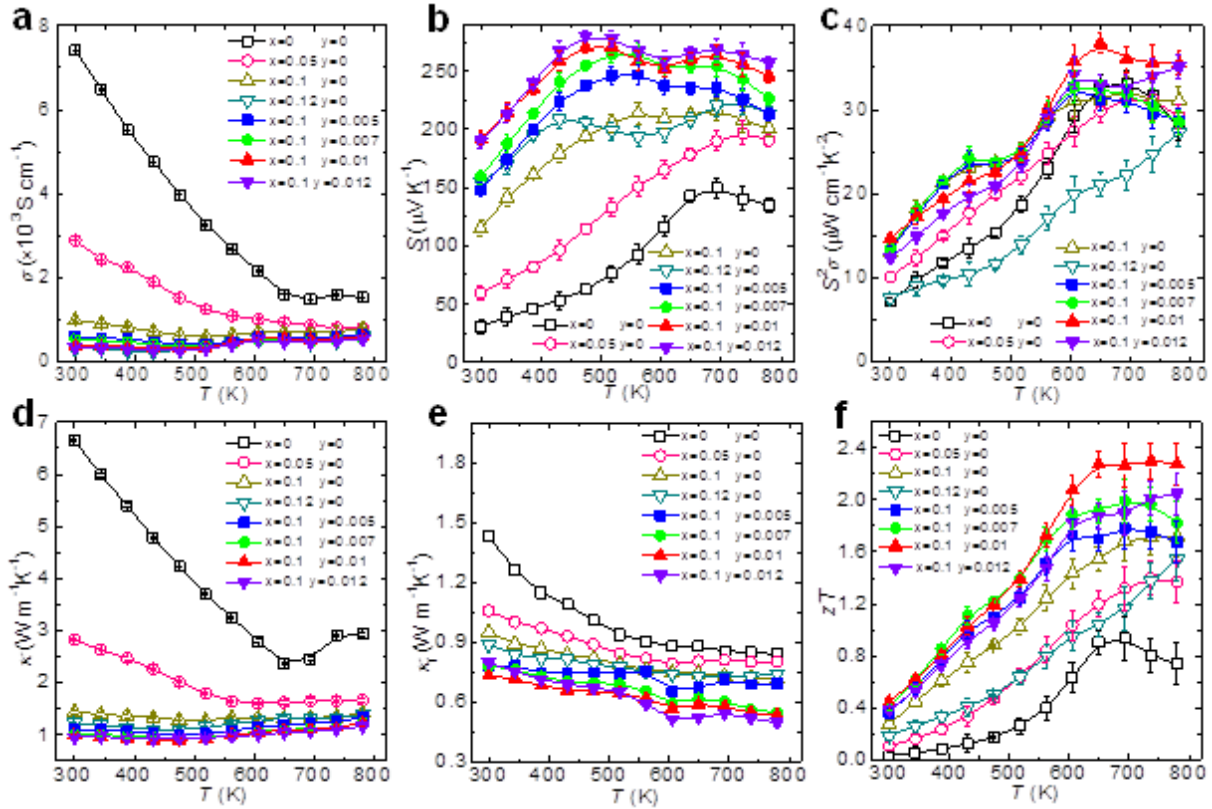
Figure 2 Thermoelectric characteristics of $Ge_{1-x-y}Sb_xIn_yTe$ over temperature range between 300 and 780 K. (a) Electrical conductivity (σ), (b) Seebeck coefficient (S), (c) thermal conductivity (κ), (d) derived lattice thermal conductivity (κ_l), (e) power-factor ($S^2\sigma$), and (f) figure-of-merit (zT).

To examine electronic transport coefficients, we quantitatively analyze the n_H-dependent data points for R-GeTe (at 300 K) and C-GeTe (at 780 K). Figure 3 shows the calculated curves of S, $S^2\sigma$, and zT as a function of n_H using the models considering $CB+VB_\Sigma$ and $CB+VB_\Sigma+VB_L$ for R-GeTe and C-GeTe, respectively (Details of the calculation method are described in Section 1, Supporting Information). Our experimental results and data points obtained from the literature (namely $Ge_{1-x}Sb_xTe$[33] and $Ge_{1-x}Bi_xTe$[28]) are also included for comparison. At 300 K (corresponding to R-GeTe, top panels of Figure 3a-c), data points of GeTe without the In doping generally follow the curves calculated using the $CB+VB_\Sigma$ model. In contrast, at 780 K (corresponding to C-GeTe, bottom panels of Figure 3a-c), the data points of GeTe without the In doping agree with the curves calculated using the $CB+VB_\Sigma+VB_L$ model and are higher than the corresponding curves calculated using the $CB+VB_\Sigma$ model. This observation suggests that the enhancement in electronic transport coefficients for C-GeTe is mainly contributed by VB_L.
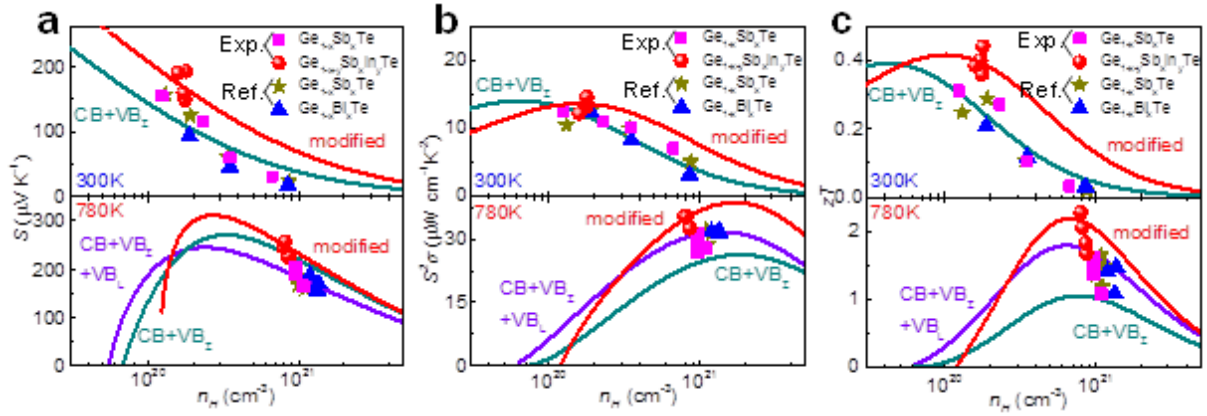
Figure 3 Analysis of electronic transport coefficients. (a), (b), and (c) calculated curve of Seebeck coefficient (S), power-factor ($S^2\sigma$), and figure-of-merit (zT) as a function of Hall carrier concentration (n_H) compared with the measured data points *versus* n_H at 300 K corresponding to rhombohedral (R-) GeTe and at 780 K corresponding to cubic (C-) GeTe. Reference data of $Ge_{1-x}Sb_xTe$[33] and $Ge_{1-x}Bi_xTe$[28] are also included. The calculated curves are based on a two-band model of conduction band plus Σ valence band (VB_C+VB_Σ) and a three-band model of conduction band plus Σ and L valence band ($VB_C+VB_\Sigma+VB_L$) for R- and C-GeTe, respectively.

In addition, this observation also suggests that the Sb doping does not substantially alter the VB structure including band effective mass (m_b^*) and ΔE of GeTe. However, there are discrepancies between these calculated curves and the data points (red balls) taken from our $Ge_{1-x-y}Sb_xIn_yTe$ materials (when In doping is considered). Especially, higher data points of S *versus* n_H for $Ge_{1-x-y}Sb_xIn_yTe$ than the correspondingly calculated curves (purple plots) indicates the increase of m_b^* due to the In doping (Figure 3a). Through modifying parameters of the primary VB, mainly increasing m_b^* by ~ 10 %, the modified S plots (red curves) can well predict the data points (red balls) of our $Ge_{1-x-y}Sb_xIn_yTe$ sample at both 300 K and 780 K. The calculated DOS for $Ge_{0.99}In_{0.01}Te$ with a distortion near the E_f (refer to Figure S4, Supporting Information) indicates that In is a type of resonant energy level dopant for both R-GeTe and C-GeTe, which agrees with the literature.[32] In response to the distorted DOS near E_f, m_b^* of the primary VB increases. Quantitatively, the modified three-band model (red curves) can fit the data points (red balls) for $Ge_{1-x-y}Sb_xIn_yTe$, which confirms the effectiveness of the resonant energy level doping for enhancing thermoelectric performance in our GeTe material, similar to that reported In-doped SnTe[40] and Tl-doped PbTe,[7] which show extraordinary thermoelectric performance.

Besides, we determine DOS effective mass (m_d^*) and deformation potential based on a single Kane band model,[29] in which parameters determining electronic transports can be deemed as the weighted summary of tensors from each individual band, as shown in Figure S11 (Supporting Information). It should be noted that the determined m_d^* for $Ge_{1-x}Sb_xTe$ shows a minor change with increasing the Sb content at a given temperature, while m_d^* increases with increasing the In content in $Ge_{1-x-y}Sb_xIn_yTe$. This further verifies the observation that In-induced distortion in DOS may enhance the thermoelectric performance of $Ge_{0.89}Sb_{0.1}In_{0.01}Te$.

It is clear that micro/nano structures affect phonon transport significantly. We therefore performed TEM characterization of the microstructure to understand the structural characteristics of the sintered $Ge_{0.89}Sb_{0.1}In_{0.01}Te$ pellet, as a typical example. Figure 4a is a TEM image, revealing the multi-grain feature, the presence of nanoscale precipitates, and a high-density of stripes. To examine the compositional difference between the matrix and precipitates, we apply the energy-dispersive X-ray spectroscopy (EDS). Figure 4b shows the EDS profiles taken from the areas that are labeled in Figure 4a. The matrix contains the Ge, Sb, In and Te peaks (note that the Cu peaks are due to the Cu grid used to support the TEM specimen and the C peak is due to slight contamination), while the precipitate consists only of Ge. Figure 4c is a high-resolution TEM (HRTEM) image taken from a typical precipitate with inset showing the corresponding selected area electron diffraction (SAED) pattern. The quantitative analysis indicates their atomic ratio (%) of Ge:Sb:In:Te roughly equaling 43.9:5.3:0.7:50.1. By contrast, the combination of HRTEM and SAED pattern illustrates that the precipitate is the face-centered cubic structured Ge. Figure 4d is an HRTEM image with inset showing the corresponding SAED pattern taken from the striped area, suggesting that the strips are stacking faults lying on their (001) basal planes.
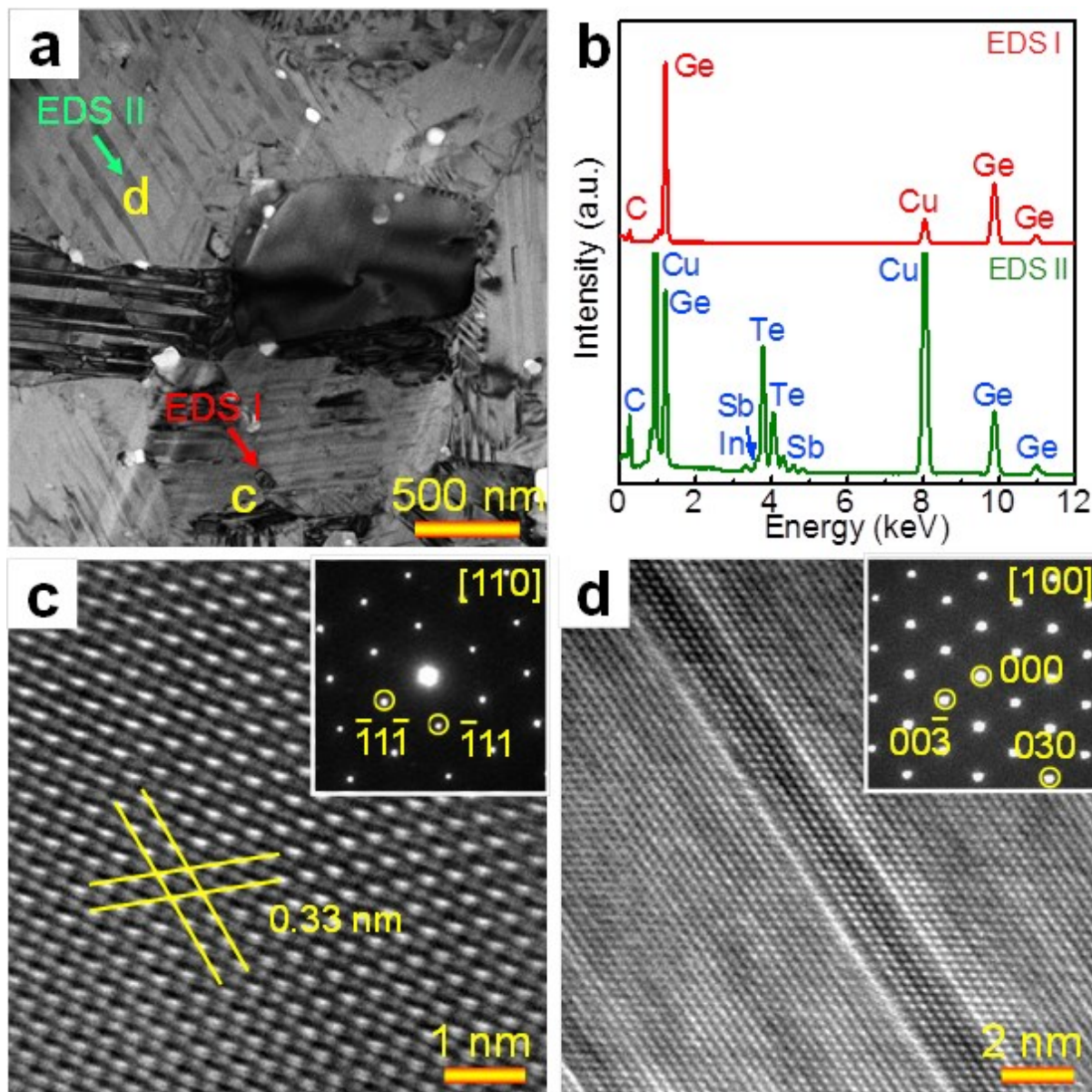
Figure 4 Transmission electron microscopy (TEM) examination of microstructures of the sintered $Ge_{0.89}Sb_{0.1}In_{0.01}Te$ pellet. (a) Low-magnification TEM image. (b) Energy-dispersive X-ray spectroscopy (EDS) profiles taken from the arrowed areas in (a). (c) and (d) HRTEM images respectively taken from the arrowed precipitate and matrix in (a) with insets showing the corresponding selected area electron diffraction (SAED) patterns.

We apply DFT calculations to examine phonon dynamics and phonon transport properties for both R-GeTe and C-GeTe. Note that we use the lattice parameters of R-GeTe and C-GeTe determined from the in-situ heated XRD patterns to perform DFT calculations. Figure 5a and b respectively depict the calculated phonon dispersions for R-GeTe and C-GeTe. The three lowest phonon branches are seen at the Γ point and they can be indexed as acoustic phonon branches, *i.e.* the out-of-plane acoustic mode (ZA), the in-plane transverse acoustic mode (TA), and the in-plane longitudinal acoustic mode

(LA).[41] While the phonon dispersion of R-GeTe shows real frequencies across the Brillouin zone, the phonon dispersion of C-GeTe displays imaginary modes along the line of (0.115 0.229 0.115) to Γ to (0.192 0 0.192), with the primary soft modes at the Γ point. We also calculate phonon dispersions of C-GeTe with different lattice parameters, allowing variation by ± 5 % (as shown in Figure S13, Supporting Information), in which imaginary modes still exist near the Γ point. The indelible imaginary modes indicate the thermodynamic instability of C-GeTe, which is the reason for the absence of C-GeTe near room temperature.

From the calculated phonon DOS of C-GeTe over the full frequency range (shown in Figure S14, Supporting Information), the imaginary modes correspond to an extremely low phonon DOS, indicating that these imaginary modes are confined to a small volume in the reciprocal space. Therefore, these imaginary modes make an almost negligible contribution to the thermal transport. Moreover, compared with R-GeTe, the phonon DOS of C-GeTe manifests a noticeable redshift, indicating a substantial phonon softening (Figure 5c).[41] Correspondingly, the frequency-dependent cumulative κ_l demonstrates that low-frequency modes contribute a larger proportion of thermal transport in C-GeTe than that in R-GeTe.
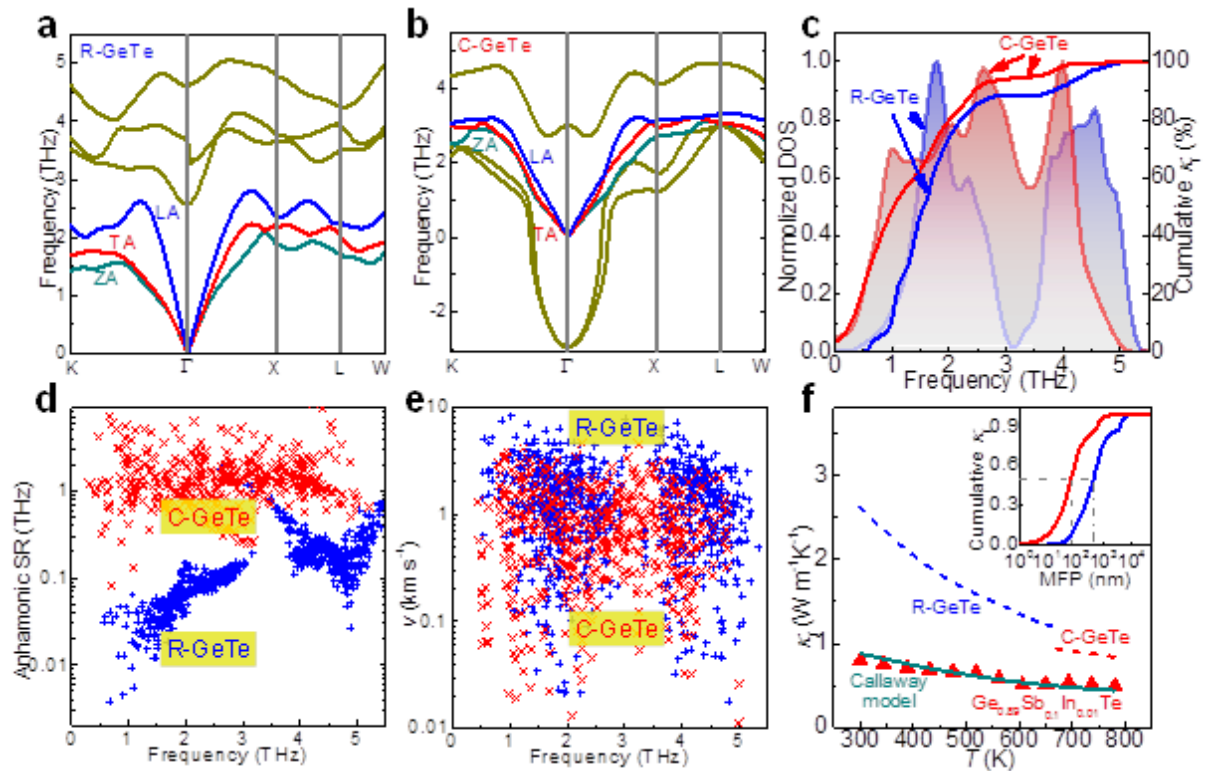

Figure 5 Density functional theory (DFT) calculations of phonon dynamics and transport properties. Phonon dispersions for (a) rhombohedral (R-) GeTe and (b) cubic (C-) GeTe. (c) Normalized phonon density of states (DOS) and the overlaid frequency-dependent cumulative lattice thermal conductivity (κ_l) for R- and C-GeTe at 300 K. (d) Anharmonic scattering rates (SRs) for R- and C-GeTe at 300 K. (e) Group velocity (v) for R- and C-GeTe at 300 K. (f) Calculated intrinsic κ_l from phonon dynamics for R- and C-GeTe, and calculated κ_l by the Callaway model including various phonon scattering mechanisms compared with the experimental data points of $Ge_{0.89}Sb_{0.1}In_{0.01}Te$ as a

function of temperature with inset showing the normalized cumulative κ_l over phonon mean free paths (MFPs) between 1 nm and 10 μm at 300 K.

A further detailed analysis of phonon-phonon interactions has also been performed. Figure 5d shows the anharmonic scattering rates (SRs) for R-GeTe (blue plus signs) and C-GeTe (red crosse signs). Anharmonic SRs is stronger in C-GeTe, indicating the strengthened anharmonic phonon-phonon interactions in this material, which can be attributed to the stereochemically active lone pair s^2 in C-GeTe.[42]

The phonon group velocity (v) is another key factor to determine κ_l, plotted in Figure 5e, from which v is generally smaller in C-GeTe. The coordination number of C-GeTe is six, doubling that of R-GeTe, and Ge-Te bonding of C-GeTe is longer than that of R-GeTe leading to a weaker bond, both of which assist in explaining the smaller v in C-GeTe.[37] The higher anharmonic SRs and smaller v can intrinsically ensure a lower κ_l in C-GeTe, as demonstrated in Figure 5f. Therefore, reducing T_c can secure a low κ_l by extending the phonon transport benefits provided by C-GeTe to lower temperatures.

To demonstrate the size effect on reducing κ_l, we have plotted the accumulative κ_l with respect to the phonon mean free path (MFP) at 300 K in the inset of Figure 5f. κ_l shifts to lower phonon MFP in C-GeTe. Qualitatively, as marked by the dash grey lines, the representative MFP (rMFP) corresponding to 50% of accumulated κ_l is 500 nm and 50 nm for R-GeTe and C-GeTe, respectively. This shows that nanostructuring, including the reduction of grain size and the introduction of nanoscale precipitates, can be an effective approach to decrease κ_l for C-GeTe.

In order to qualitatively study how the observed micro/nano structures affect thermal transport within $Ge_{0.89}Sb_{0.1}In_{0.01}Te$, we calculated κ_l using the Callaway model by considering various phonon scattering mechanisms, including Umklapp processes, grain boundaries, point defects, and stacking faults (refer to Section 12 of Supporting Information for the detailed calculation method).[13,43,44] The results are shown as the green solid curve in Figure 5f, from which the calculated κ_l may well predict the experimental κ_l as a function of temperature for $Ge_{0.89}Sb_{0.1}In_{0.01}Te$, deviating from the calculated intrinsic κ_l for either R-GeTe (blue dash curve) or C-GeTe (red dash curve). This observation suggests that the low κ_l of $Ge_{0.89}Sb_{0.1}In_{0.01}Te$ is due to the intrinsically dampened phonon transport within C-GeTe, along with the extrinsically strengthened phonon scattering due to grain boundaries, nanoscale precipitates, stacking faults, and point defects.

In summary, we have realized a $zT \approx 2.3$ in $Ge_{0.89}Sb_{0.1}In_{0.01}Te$, which is associated with the enhanced $S^2\sigma$ and the decreased κ. Electrically, DFT calculations in conjunction with modeling study demonstrate and explain the superior electronic transport coefficients of pristine GeTe, due to the presence of two valence bands with reduced energy offset in C-GeTe. The evolution of Ge s2 lone pair electrons is responsible for the presence of two valence bands in C-GeTe. In addition, In is confirmed to be an effective resonant dopant for both R-GeTe and C-GeTe in order to induce the distortion of DOS near E_f. Accordingly, the experimental $S^2\sigma$ is remarkably enhanced by In doping, providing the optimized n by the Sb doping. Thermally, as revealed by phonon dynamic studies, C-

GeTe has stronger anharmonic phonon-phonon interactions and smaller phonon group velocity than R-GeTe. TEM studies demonstrated that the presence of grain boundaries, a high density of stacking faults, and nanoscale precipitates, which in conjunction with inevitable point defects lead to extrinsically strong phonon scatterings. The intrinsically dampened phonon transport and extrinsically enhanced phonon scatterings result in a decreased κ. This study provides significant fundamental insights and extraordinary experimental progress in GeTe, which encourages possible further thermoelectric enhancement in p-type Pb-free GeTe derivatives via band convergence using doping and strengthening phonon scattering by nanostructuring.

Experimental Section

Material Synthesis: In this study, high-purity elemental Ge, Sb, In, and Te, purchased from Sigma-Aldrich, were utilized as precursors. To synthesize $Ge_{1-x-y}Sb_xIn_yTe$ alloys, precursors were sealed in fused quartz tubes under vacuum. Quartz tubes were heated to 1223 K slowly (in 12 h), and held for 6 h, followed by quenching in ice water. Samples were then annealed at 923 K for 3 days. The resulting ingots were ball-milled for 10 minutes into fine powders and consolidated by spark plasma sintering under a pressure of 55 MPa at 550 ˚C for 5 min under vacuum. The densities of all sintered pellets were confirmed to be ~ 98 % of the theoretical density for GeTe by the Archimedes method.

Characterization: The phase purities of as-synthesized samples were characterized by XRD, recorded on an X-ray diffractometer (Bruker D8 Advance MKII) equipped with graphite monochromatized, Cu Kα radiation (λ = 1.5418 Å). The *in-situ* heated XRD characterization was performed using the Rigaku SmartLab over 300 K to 800 K under vacuum. The DSC profiles were collected using DSC 404F3 NETZSCH with a heating and cooling rate of 10 K/min from room temperature to 780 K. The structural and chemical characteristics of the sintered pellets were investigated by TEM (Philips Tecnai F20, equipped with EDS for compositional analysis).

Thermoelectric Property Measurement: Thermal diffusivity (D) was measured by a laser flash method (LFA 457, NETZSCH), and κ was calculated using $\kappa = DC_pd$, where C_p and d are the specific heat capacity and density, respectively. C_P was determined using the Dulong-Petit law, which has been widely used in GeTe systems.[28,32,33,45,46] σ and S were measured simultaneously on a ZEM-3, ULVAC. The Hall coefficient (R_H) was measured using the Van der Pauw method in a magnetic field up to ±1.5T.[47] n_H and Hall carrier mobility (μ_H) were respectively calculated using $n_H = 1/(eR_H)$ and $\mu_H = \sigma R_H$ with e representing the electron charge.

Density Functional Theory Calculations: Band structure calculations were performed using the plane-wave self-consistent field (PWSCF) code, and phonon dispersion relations were calculated by means of density functional perturbation theory (DFPT)[48] as implemented in the QUANTUM-ESPRESSO suite of programs.[49] The exchange and correlation interactions were described using the local density approximation (LDA).[50] Values of 60 and 280 Ry were chosen as the cut-offs for the selection of the plane-wave basis sets for describing the kinetic energy and the electronic density, respectively. The spin-orbit interaction was included during the calculation, and the structures were fully relaxed until the force on each atom was less than 10^{-5} eV Å^{-1}. We used a uniform mesh of 9×9×9 k-points in sampling integrations over the Brillouin zone for the band structure, DOS, and phonon dispersion of R-GeTe and C-GeTe. Calculation for DOS of $Ge_{0.99}TeIn_{0.01}$ was performed by

replacing one Ge site with In atoms in a 3×3×3 supercell of $Ge_{108}Te_{108}$ which used a uniform mesh of 2×2×2 k-points. The phonon dynamics and intrinsic thermal conductivity of R- GeTe and C-GeTe were calculated by considering only the phonon-phonon scattering and solving the semi-classical phonon Boltzmann transport equation (BTE) iteratively using the ShengBTE package.[51] The second-order harmonic interatomic force constants (IFCs) were obtained within the linear response framework by employing DFPT, performed using QUANTUM-ESPRESSO. The third-order anharmonic IFCs were calculated using ShengBTE, in which we used a 4×4×4 supercell with a uniform mesh of 2×2×2 k-points.

Supporting Information

Supporting Information is available from the Wiley Online Library or from the author.

Acknowledgements

References

[1] Y. Pei, X. Shi, A. LaLonde, H. Wang, L. Chen, G. J. Snyder, *Nature* **2011**, *473*, 66.

[2] L.-D. Zhao, G. Tan, S. Hao, J. He, Y. Pei, H. Chi, H. Wang, S. Gong, H. Xu, V. P. Dravid, C. Uher, G. J. Snyder, C. Wolverton, M. G. Kanatzidis, *Science* **2016**, *351*, 141.

[3] T. Zhu, Y. Liu, C. Fu, J. P. Heremans, J. G. Snyder, X. Zhao, *Adv. Mater.* **2017**, *29*, 1605884.

[4] H. Liu, X. Shi, F. Xu, L. Zhang, W. Zhang, L. Chen, Q. Li, C. Uher, T. Day, G. J. Snyder, *Nat. Mater.* **2012**, *11*, 422.

[5] K. Peng, X. Lu, H. Zhan, S. Hui, X. Tang, G. Wang, J. Dai, C. Uher, G. Wang, X. Zhou, *Energy Environ. Sci.* **2015**, *9*, 454.

[6] J. P. Heremans, V. Jovovic, E. S. Toberer, A. Saramat, K. Kurosaki, A. Charoenphakdee, S. Yamanaka, G. J. Snyder, *Science* **2008**, *321*, 554.

[7]   H. Yang, J.-H. Bahk, T. Day, A. M. S. Mohammed, G. J. Snyder, A. Shakouri, Y. Wu, *Nano Lett.* **2015**, *15*, 1349.

[8]   Z.-G. Chen, G. Han, L. Yang, L. Cheng, J. Zou, *Prog. Nat. Sci.* **2012**, *22*, 535.

[9]   Y. Pei, C. Chang, Z. Wang, M. Yin, M. Wu, G. Tan, H. Wu, Y. Chen, L. Zheng, S. Gong, T. Zhu, X. Zhao, L. Huang, J. He, M. G. Kanatzidis, L.-D. Zhao, *J. Am. Chem. Soc.* **2016**, *138*, 16364.

[10]   S. Wang, Y. Sun, J. Yang, B. Duan, L. Wu, W. Zhang, J. Yang, *Energy Environ. Sci.* **2016**, *9*, 3436.

[11]   M. Hong, Z.-G. Chen, L. Yang, T. C. Chasapis, S. D. Kang, Y. Zou, G. J. Auchterlonie, M. G. Kanatzidis, G. J. Snyder, J. Zou, *J. Mater. Chem. A* **2017**, *5*, 10713.

[12]   L. Yang, Z.-G. Chen, G. Han, M. Hong, Y. Zou, J. Zou, *Nano Energy* **2015**, *16*, 367.

[13]   M. Hong, T. C. Chasapis, Z.-G. Chen, L. Yang, M. G. Kanatzidis, G. J. Snyder, J. Zou, *ACS Nano* **2016**, *10*, 4719.

[14]   S. Wang, J. Yang, L. Wu, P. Wei, W. Zhang, J. Yang, *Adv. Funct. Mater.* **2015**, *25*, 6660.

[15]   J. Shuai, J. Mao, S. Song, Q. Zhu, J. Sun, Y. Wang, R. He, J. Zhou, G. Chen, D. J. Singh, Z. Ren, *Energy Environ. Sci.* **2017**, *10*, 799.

[16]   S. Perumal, S. Roychowdhury, D. S. Negi, R. Datta, K. Biswas, *Chem. Mater.* **2015**, *27*, 7171.

[17]   L. Zhao, S. H. Lo, Y. Zhang, H. Sun, G. Tan, C. Uher, C. Wolverton, V. P. Dravid, M. G. Kanatzidis, *Nature* **2014**, *508*, 373.

[18]   M. G. Kanatzidis, *Chem. Mater.* **2010**, *22*, 648.

[19]   G. Zhang, B. Kirk, L. A. Jauregui, H. Yang, X. Xu, Y. P. Chen, Y. Wu, *Nano Lett.* **2012**, *12*, 56.

[20]   H. Fang, T. Feng, H. Yang, X. Ruan, Y. Wu, *Nano Lett.* **2013**, *13*, 2058.

[21]   H. Fang, H. Yang, Y. Wu, *Chem. Mater.* **2014**, *26*, 3322.

[22]   K. Biswas, J. He, I. D. Blum, C. I. Wu, T. P. Hogan, D. N. Seidman, V. P. Dravid, M. G. Kanatzidis, *Nature* **2012**, *489*, 414.

[23]   L.-D. Zhao, V. P. Dravid, M. G. Kanatzidis, *Energy Environ. Sci.* **2014**, *7*, 251.

[24]   R. Moshwan, L. Yang, J. Zou, Z.-G. Chen, *Adv. Funct. Mater.* **2017**, 10.1002/adfm.201703278.

[25]   L. Yang, Z.-G. Chen, M. S. Dargusch, J. Zou, *Adv. Energy Mater.* **2017**, 10.1002/aenm.201701797.

[26]   S. Perumal, S. Roychowdhury, K. Biswas, *J. Mater. Chem. C* **2016**, *4*, 7520.

[27]   T. Chatterji, C. M. N. Kumar, U. D. Wdowik, *Phys. Rev. B* **2015**, *91*, 054110.

[28]   J. Li, Z. Chen, X. Zhang, Y. Sun, J. Yang, Y. Pei, *NPG Asia Mater.* **2017**, *9*, e353.

[29]   M. Hong, Z.-G. Chen, Y. Pei, L. Yang, J. Zou, *Phys. Rev. B* **2016**, *94*, 161201.

[30]   Y. Pei, H. Wang, G. J. Snyder, *Adv. Mater.* **2012**, *24*, 6125.

[31]   W. Li, L. Zheng, B. Ge, S. Lin, X. Zhang, Z. Chen, Y. Chang, Y. Pei, *Adv. Mater.* **2017**, *29*, 1605887.

[32]   L. Wu, X. Li, S. Wang, T. Zhang, J. Yang, W. Zhang, L. Chen, J. Yang, *NPG Asia Mater.* **2017**, *9*, e343.

[33]   J. Li, X. Zhang, S. Lin, Z. Chen, Y. Pei, *Chem. Mater.* **2016**, *29*, 605.

[34]   D. Di Sante, P. Barone, R. Bertacco, S. Picozzi, *Adv. Mater.* **2013**, *25*, 509.

[35]   K. Hoang, S. D. Mahanti, M. G. Kanatzidis, *Phys. Rev. B* **2010**, *81*, 115106.

[36]   Z. M. Gibbs, H.-S. Kim, H. Wang, G. J. Snyder, *Appl. Phys. Lett.* **2015**, *106*, 022112.

[37]   W. G. Zeier, A. Zevalkink, Z. M. Gibbs, G. Hautier, M. G. Kanatzidis, G. J. Snyder, *Angew. Chem. Int. Edit.* **2016**, *55*, 6826.

[38]   D. Wu, L. Zhao, S. Hao, Q. Jiang, F. Zheng, J. W. Doak, H. Wu, H. Chi, Y. Gelbstein, C. Uher, C. Wolverton, M. Kanatzidis, J. He, *J. Am. Chem. Soc.* **2014**, *136*, 11412.

[39]   M. Hong, Z. G. Chen, L. Yang, J. Zou, *Nano Energy* **2016**, *20*, 144.

[40]   Q. Zhang, B. Liao, Y. Lan, K. Lukas, W. Liu, K. Esfarjani, C. Opeil, D. Broido, G. Chen, Z. Ren, *Proc. Natl. Acad. Sci. USA* **2013**, *110*, 13261.

[41]   J. M. Skelton, L. A. Burton, S. C. Parker, A. Walsh, C.-E. Kim, A. Soon, J. Buckeridge, A. A. Sokol, C. R. A. Catlow, A. Togo, I. Tanaka, *Phys. Rev. Lett.* **2016**, *117*, 075502.

[42]   M. D. Nielsen, V. Ozolins, J. P. Heremans, *Energy Environ. Sci.* **2013**, *6*, 570.

[43]   S. I. Kim, K. H. Lee, H. A. Mun, H. S. Kim, S. W. Hwang, J. W. Roh, D. J. Yang, W. H. Shin, X. S. Li, Y. H. Lee, G. J. Snyder, S. W. Kim, *Science* **2015**, *348*, 109.

[44]   M. Hong, Z.-G. Chen, L. Yang, Z.-M. Liao, Y.-C. Zou, Y.-H. Chen, S. Matsumur, J. Zou, *Adv. Energy Mater.* **2017**, 10.1002/aenm.201702333.

[45]   M. Samanta, K. Biswas, *J. Am. Chem. Soc.* **2017**, *139*, 9382.

[46]   F. Fahrnbauer, D. Souchay, G. Wagner, O. Oeckler, *J. Am. Chem. Soc.* **2015**, *137*, 12633.

[47]   K. A. Borup, E. S. Toberer, L. D. Zoltan, G. Nakatsukasa, M. Errico, J.-P. Fleurial, B. B. Iversen, G. J. Snyder, *Rev. Sci. Instrum.* **2012**, *83*, 123902.

[48]   S. Baroni, S. de Gironcoli, A. Dal Corso, P. Giannozzi, *Rev. Mod. Phys.* **2001**, *73*, 515.

[49]   P. Giannozzi, S. Baroni, N. Bonini, M. Calandra, R. Car, C. Cavazzoni, D. Ceresoli, G. L. Chiarotti, M. Cococcioni, I. Dabo, A. D. Corso, S. d. Gironcoli, S. Fabris, G. Fratesi, R. Gebauer, U. Gerstmann, C. Gougoussis, A. Kokalj, M. Lazzeri, L. Martin-Samos, N. Marzari, F. Mauri, R. Mazzarello, S. Paolini, A. Pasquarello, L. Paulatto, C. Sbraccia, S. Scandolo, G. Sclauzero, A. P. Seitsonen, A. Smogunov, P. Umari, R. M. Wentzcovitch, *J. Phys. Condens. Matter.* **2009**, *21*, 395502.

[50]   J. P. Perdew, K. Burke, M. Ernzerhof, *Phys. Rev. Lett.* **1996**, *77*, 3865.

[51]   W. Li, J. Carrete, N. A. Katcho, N. Mingo, *Comput. Phys. Commun.* **2014**, *185*, 1747.

The table of contents entry

An ultra-high figure-of-merit of 2.3 is achieved in $Ge_{0.89}Sb_{0.1}In_{0.01}Te$ through enhanced power-factor and decreased thermal conductivity. The enhanced power-factor is caused by the optimized carrier concentration, reduced phase-transition temperature, and introduced resonant-energy doping. The decreased thermal conductivity is due to the enhanced phonon scatterings by the intrinsically deformed phonon transport and the externally induced phonon scattering sources.

Keywords

GeTe alloys, thermoelectric, phase transition, density-functional-theory calculations, phonon dynamics

Author

Min Hong, Zhi-Gang Chen,* Lei Yang, Yi-Chao Zou, Matthew S. Dargusch, Hao Wang, and Jin Zou*

Title

Realizing $zT > 2.3$ in $Ge_{1-x-y}Sb_xIn_yTe$ via Reducing the Phase-Transition Temperature and Introducing Resonant Energy Doping

ToC figure